Microbial redox cycling enhances ecosystem thermodynamic efficiency and productivity

[a*]Mayumi Seto and [b*]Michio Kondoh

Affiliations:
[a]*Department of Chemistry, Biology, and Environmental Sciences, Nara Women's University, Kita-Uoya Nishimachi, Nara 630-8506, Japan*
seto@ics.nara-wu.ac.jp

[b]*Graduate School of Life Sciences, Tohoku University, 6-3 Aramaki Aza Aoba, Aoba-ku, Sendai 980-8578, Japan*

Running Title: Microbial redox cycling: Eco-redox model

Keywords:
division of labor, mutualism, community network, microbial ecology, population dynamics, thermodynamics, niche construction, material cycle, redox chemistry, biogeochemistry

Type of Article: Letter

Data availability

If the manuscript is accepted, data supporting the results will be archived in Dryad and the data DOI will be included at the end of the article.

Furthermore, we provide all the information needed to replicate the simulations in Supplemental Information. All codes were written in the Wolfram Language platform using Mathematica 12. The codes are available in Example.nb. See details in Section S2.2.

Number of

Words in the abstract	Words in the main text	References	Figures	Tables	Text boxes
140	4526	40	6	0	0

Statement of authorship

M.S and M.K conceived of the presented idea. M.S designed the model and the computational framework and analyzed the data. M.S and M.K contributed equally to the interpretation of the results and writing the manuscript.

Abstract

Microbial life in an ecosystem with low energy supply has been considered to employ two energy utilization strategies. The first is energy conservation at an individual level, while the second is energy use optimization in response to the availability of energy resources. Here, using an oxidation-reduction (redox) reaction network model where microbial metabolic pathways are established through multiple species-level competition and cooperation within a redox reaction network, we hypothesize that microbial ecosystems can move forward to increase energy use efficiency, namely an energy efficiency strategy at the community level. This strategy is supported by microbial functional diversity that enables species to interact with others in various ways of metabolic handoffs. Moreover, the high energy use efficiency is attributable to the mutualistic division of labor that increases the complexity of metabolic pathways, which actively drives material cycling to exploit more energy.

Introduction

All life on Earth relies on ATP as the primary energy carrier, and its production and transfer significantly depend on the ecosystems' electron transfer potential. In the surface ecosystems, sunlight fuels electron transfer for ATP synthesis via photosynthesis, following which aerobic respirators harvest chemical energy by transferring electrons stored in organic carbon to oxygen in a redox reaction. Aerobic respiration and various of redox reactions (e.g., denitrification, iron oxidation, and methanogenesis) supply power to prokaryotic organisms. In particular, inorganic redox reactions must have been the fundamental energy sources for life before the evolution of photosynthesis. In the subsurface realm, which replicates the conditions of the early Earth where organic carbon and oxygen were not readily available, the power available for microbes is significantly limited compared with that in surface ecosystems (Momper *et al.* 2017; Bradley *et al.* 2020). Nevertheless, the microbial biomass in the subsurface today is several to tens of PgC (Kallmeyer *et al.* 2012; Bar-On *et al.* 2018; Magnabosco *et al.* 2018), comprising nearly 70% of the overall microbial cells on Earth (Flemming & Wuertz 2019). Thus, it remains a mystery as to how these microbial communities maintain their productivity in energetically (or thermodynamically) less favorable environments (Hoehler & Jørgensen 2013a; Starnawski *et al.* 2017).

One adaptive strategy for microorganisms harbored in such environments is the conservation of energy at the individual level. Indeed, subsurface microorganisms appear to minimize energy expense to maintain their vital functions until sufficient energy for growth becomes available (Jørgensen & Boetius 2007; Morono *et al.* 2011; Hoehler & Jørgensen 2013b). Another strategy is to optimize the energy exploitation in response to the change in resource influx. Fermentation, the partial breakdown of

organic carbon, produces less ATP per organic carbon than that produced by aerobic respiration, which involves the complete oxidation of organic carbon to carbon dioxide. Although fermentation is thermodynamically less favorable than aerobic respiration, fermentation can produce more ATP per time at higher organic carbon influx rates owing to the trade-off between the yield and rate of ATP production (Pfeiffer *et al.* 2001; Kreft *et al.* 2020). Experimental, observational, and metagenomic evidence supports that microbes often sequentially proceed with incomplete reactions that are generally less thermodynamically favorable than a complete reaction wherein they divide metabolic labor within the community by exchanging reaction byproducts (excreted metabolites) or even electrons directly from one to another (McInerney *et al.* 2009; Morris *et al.* 2013; Embree *et al.* 2015; Kouzuma *et al.* 2015; Anantharaman *et al.* 2016). This so-called division of metabolic labor also seems to be related to the energy utilization efficiency of microbial communities. However, it is unclear whether such a division of labor can be advantageous and increase energy utilization efficiency at the community level within a redox network where various microbial reactions and interactions are entangled with each other.

To address this question, we developed an eco-redox model, a microbial community network model based on thermodynamic and redox properties. We found that, without assuming a trade-off between the yield and rate of ATP production, species that mutually divide the metabolic labor and enhance material cycling can replace species harnessing energetically more favorable reactions. Thermodynamic calculations suggest

that a microbial community composed of a mutualistic division of labor is endowed with higher energy utilization efficiency and productivity. Furthermore, we found that microbial ecosystems with metabolic functional diversity can move forward to increase the energy utilization efficiency and productivity.

Methods

Eco-redox model

We constructed a conceptual model that explicitly links population dynamics to the redox process within the general framework of thermodynamics and redox chemistry to build a theoretical foundation that integrates the dynamics of microbial community and redox reaction network (Fig. 1). The electron fluxes in geochemical cycles on Earth are mainly driven by the chemical substances of C, N, S, Fe, Mn, O, and H (Falkowski *et al.* 2008). In our model, each chemical substance involving a redox network was denoted by X_j, where X indicates a characteristic element (X = A, B, C, …) and j is the relative number of electrons that X holds ($1 \leq j \leq N_X$). j is not exactly equal to the actual oxidation state but shows the relative electron density; X_1 possesses the lowest electron density within the X-bearing substances present in the system. For instance, for nitrogen-bearing substances as an example, when X_1 is N_2, NH_2OH, N_2H_4, and NH_3 (or NH_4^+) can correspond to X_2, X_3, and X_4, respectively. Assuming that no chemical substances with the same oxidation state of X exists in a system and the half-reaction $X_j + (z-j)e^- \rightleftharpoons X_z$ holds (where $j < z$ and e^- denotes an electron), a redox network template was designed using all possible combinations of two half-reactions

(an oxidation reaction losing electrons and a reduction reaction gaining electrons) in the system (see Supporting Information Section S1). The topological structure of a redox network and the number of possible redox reactions forming the network (N_{reac}) were uniquely determined for a given N_{tot} chemical substances (Fig. 1a). Each of the smaller vertexes in Fig. 1a show a possible forward and backward redox reaction, which converts the given reactants into given products via edges (Fig. 1a). Although not all redox reactions in natural systems are confirmed to be utilized as microbial energy sources (Kuypers *et al.* 2018), all redox reactions forming the redox network template are assumed to be available for microbes to harness. In other words, the metabolic diversity of a community determines the complexity of the redox network template.

Within the network, the thermodynamic (energetic) advantage of a reaction was characterized in terms of the Gibbs energy utilized per reaction (Fig. 1b). The amount of Gibbs energy associated with the chemical substances of all X_j was defined as $G = V\sum[X_j]\mu_{X_j}$ where V, $[X_j]$, and μ_{X_j} denote the volume of the system (L), the molar concentration of X_j (mol L^{-1}), and the chemical potential of X_j (kJ mol^{-1}), respectively. The negative value of the Gibbs energy change of the ith reaction ($-\Delta_r G_i$ [kJ mol^{-1}]) designates the maximum energy supply per reactant available for a microbial cell to synthesize ATP. $-\Delta_r G_1$ for reaction 1 in Fig. 1a ($A_1 + C_2 \rightharpoonup A_2 + C_1$) is determined as follows:

$$-\Delta_r G_1 = \mu_{A_1} + \mu_{C_2} - \mu_{A_2} - \mu_{C_1}$$
$$= -\Delta_r G_1^\circ + RT\ln\frac{[A_1][C_2]}{[A_2][C_1]}, \quad (1)$$

where

$$-\Delta_r G_1^\circ = \mu_{A_1}^\circ + \mu_{C_2}^\circ - \mu_{A_2}^\circ - \mu_{C_2}^\circ$$

º denotes the standard state at a specific temperature (15 ºC), pressure (1 bar), and concentration (1 mol L^{-1}); R and T are the gas constant and the absolute temperature, respectively. The activity of X_j was replaced by the molar concentration in this study.

A group of species that utilize an identical redox reaction as an energy source is hereafter referred to as a microbial species (Sp). We considered an open system where as many microbial species as N_{reac} are introduced without additional exchange of cells with the surroundings. The population dynamics of Sp i, which specifically harness reaction i for population growth, were kinetically or thermodynamically limited depending on the abundance of the reactants and the Gibbs energy:

$$\frac{dM_i}{dt} = q_i(c_i(-\Delta_r G_i)f_i - m_i)M_i, \qquad (2a)$$

where

$$f_1 = r_1 \frac{[A_1]}{K_{1,A_1}+[A_1]} \frac{[C_2]}{K_{1,C_2}+[C_2]} \quad \text{for reaction 1 in Fig 1a.} \qquad (2b)$$

M_i is the biomass of Sp i; $-\Delta_r G_i$ (kJ mol^{-1}) is the $-\Delta_r G$ of the ith reaction; f_i is the microbial catalytic rate of the ith reaction, where r_1 and K_{1,X_j} are respectively the maximum catalytic rate per biomass (mol g^{-1} h^{-1}) and the Michaelis–Menten constants (mol L^{-1}); q_i is the biomass yield per energy (g kJ^{-1}): c_i is the fraction of energy that can be used for ATP synthesis ($0 \le c_i \le 1$); and m_i is the maintenance energy of Sp i (kJ

g^{-1} h^{-1}) (Seto & Iwasa 2019a). For numerical simulations, the values of r_i and $K_{i,Xj}$ were determined independently from the thermodynamic favorability of the ith reaction without assuming the trade-off between the yield and rate of ATP production. The dynamics of the molar concentration of $[X_j]$ were determined as follows:

$$\frac{d[X_j]}{dt} = I_{X_j} - D_{X_j}[X_j] + \sum \alpha_{i,X_j} f_i M_i + \sum \alpha_{i,X_j} F_i \ , \qquad (3)$$

where I_{Xj} and D_{Xj} are the inflow rate (mol L^{-1} h^{-1}) and the outflow rate constant (h^{-1}) of X_j, respectively. The third and fourth terms denote the microbial and abiotic reaction rates where α_{i,X_j} is the stoichiometric constant of X_j in reaction i. The abiotic reaction rate (F_i) is proportional to the product of the molar concentration of the reactant(s) with the reaction rate constant k_i. Under the given different thermodynamic or microbial parameters, different pathways can be established at the steady state within the same redox network template (Fig. 1c). Microbially driven material flows among X-bearing substances may incorporate cyclic structures, which may also consist of subcycles.

Numerical simulations

We developed an algorithm in the Wolfram language in Mathematica 12, which automatically formulates the list of redox reactions and simulates the dynamics of N_{reac} Sps and N_{tot} chemical substances, once the numbers of X-bearing substances, N_X, are determined (see section S2). Two scenarios for the inflow rate of X_j (I_{X_j}) were considered: (i) the inflow rates of all X_j were uniformly increased (I_{X_j} = [Inflow rate]/N_{tot}), and (ii)

the inflow rates of only the most oxidized electron acceptors X_1 were uniformly increased (I_{X_1} = [Inflow rate] and 10^{-5} for other X_j). The scenario (i) explores the redox boundary system where both electron donors (X_j with larger j) and acceptors (X_j with smaller j) are supplied at different levels in a well-balanced manner, whereas the scenario (ii) investigates the transition from reduced to oxidized state, respectively. The redox balance of the inflow was evaluated by determining the relative oxidation number of X_j (E_{X_j}). The relative oxidation number of X_j with $j = 1$ was considered -1 and the relative oxidation number of X_j for which j is the maximum value among all X_j (j_{max}) was considered +1. The relative oxidation number of other X_j was determined as $E_{X_j} = -1 + 2/(j_{max} - 1)$. The redox balance of the inflow is given by $\sum_X \sum_j E_{X_j} I_{X_j}$.

The initial conditions of variables, default values of parameters, and ranges for random variables are summarized in Table S1. N_{tot} = 6, 7, 8, 9, 10, 11, and 12 correspond to (N_A, N_B, N_C) = (2, 2, 2), (3, 2, 2), (3, 3, 2), (3, 3, 3), (4, 3, 3), (4, 4, 3), and (4, 4, 4), respectively.

Gibbs energy at the microbes-free state and equilibrium

The thermodynamic efficiency of microbial community was evaluated by comparing the Gibbs energy characterized by microbial community activity (G_{bio}), G at the microbes-free state (G_{abio}), and the equilibrium G (G_{eq}). For a microbe-free open system, the molar concentrations of X_j were determined using the balance of exchanges of X_j with the surroundings and abiotic reaction rates. Because we only simulated the case where the input and output rates of X_j (I_{X_j} and D_{X_j}) are at least a few orders of

magnitude higher than the abiotic reaction rate constants, the molar concentration of X_j can be approximated by I_{X_j}/D_{X_j}. The steady state Gibbs energy at the microbe-free state was determined as follows:

$$G^*_{abio} = V \sum_X \sum_j \mu_{X_j} \frac{I_{X_j}}{D_{X_j}} = V \sum_X \sum_j \left(\mu_{X_j}^\circ + RT \ln \frac{I_{X_j}}{D_{X_j}} \right) \frac{I_{X_j}}{D_{X_j}}, \quad (4)$$

where * denotes a steady state.

The thermodynamic equilibrium refers to the state in which no further change occurs in an isolated system (i.e., $I_{Xj} = 0$ and $D_{Xj} = 0$ for all X_j) where all half-reactions comprising the redox network template must have reached equilibrium. For a half-reaction $X_j + e^- \rightharpoonup X_{j+1}$ ($1 \leq j \leq (N_X - 1)$), the redox reaction with a reference reaction ($1/2H_2\,(g) \rightarrow H^+ + e^-$) is as follows:

$$X_j + \frac{1}{2}H_2\,(g) \rightleftharpoons X_{j+1} + H^+. \quad (5)$$

Because the standard chemical potentials of H_2 (g) and H^+ are 0, the standard Gibbs energy change of Eq. 4 is $\Delta_r G_j^\circ = \mu_{X_{j+1}}^\circ - \mu_{X_j}^\circ$. Letting the equilibrium constant of Eq. 5 be K_j and solving $\Delta_r G_j = \Delta_r G_j^\circ + RT \ln K_j = 0$ for K_j,

$$K_j = \exp\left\{-\frac{\Delta_r G_j^\circ}{RT}\right\}. \quad (6)$$

Using Eq. 6, the equilibrium molar concentration of X_j ($j \geq 2$) satisfies

$$K_j\widehat{[\mathrm{X}_{j-1}]} = \prod_{i=1}^{j} K_i\,[\widehat{\mathrm{X}_1}] \tag{7}$$

where the hat denotes the equilibrium. Letting T_X be the total number of moles of X-bearing substances, which is conserved in the isolated system:

$$\begin{aligned} T_{\mathrm{X}} &= [\mathrm{X}_1] + [\mathrm{X}_2] + [\mathrm{X}_3] + \cdots + [\mathrm{X}_{N_X}] \\ &= [\widehat{\mathrm{X}_1}] + K_1[\widehat{\mathrm{X}_1}] + K_1K_2[\widehat{\mathrm{X}_1}] + K_1K_2K_3[\widehat{\mathrm{X}_1}] + \cdots + [\widehat{\mathrm{X}_1}]\prod_{i=1}^{N_X} K_i \\ &= [\widehat{\mathrm{X}_1}]\left(1 + \sum_{j=1}^{N_X}\prod_{i=1}^{j} K_i\right) \end{aligned} \tag{8}$$

Solving Eq. 8 for $[\widehat{\mathrm{X}_1}]$,

$$[\widehat{\mathrm{X}_1}] = \frac{T_{\mathrm{X}}}{1+\sum_{j=1}^{N_X}\prod_{i=1}^{j} K_i} \tag{9}$$

The molar concentrations of other X_j ($j \geq 2$) at equilibrium were obtained using Eq. 7. The equilibrium Gibbs energy is

$$G_{eq} = V\sum_{\mathrm{X}}\sum_j \mu_{\mathrm{X}_j}\widehat{[\mathrm{X}_j]} = V\sum_{\mathrm{X}}\sum_j \left(\mu_{\mathrm{X}_j}^{\circ} + RT\,\ln\widehat{[\mathrm{X}_j]}\right)\widehat{[\mathrm{X}_j]}. \tag{10}$$

For comparison, T_{X} and V were fixed to $\sum_j I_{\mathrm{X}_j}/D_{\mathrm{X}_j}$ for each X and 1, respectively.

Results

Co-development of the division of labor and material cycling

Analysis of the eco-redox model revealed that energetically less favorable reactions can be intensively driven by the division of labor, which is closely linked to the topological structure of microbial pathways, depending on metabolic handoffs, energy allocation, and material cycling. For a template consisting of six reactions at (N_A, N_B, N_C) = (2, 2, 2), not only each Sp in Fig. 2a competes for the same reactant at the species-level, but Sps 2 and 3 as an assembly unit also compete with Sp 1 because the consortium of Sps 2 and 3 proceed with reaction 1 by recycling B_1 and B_2 as electron carriers (Seto & Iwasa 2019b, 2020). Furthermore, Sps 2 and 3 are in a division of labor to complete reaction 1 by allocating the available Gibbs energy per reaction to each other. For a more complex redox network, the forms of division of labor are not straightforward because multiple Sps split a reaction into several ones (e.g., segmentation of $A_1 \rightarrow A_4$ into $A_1 \rightarrow A_2$, $A_2 \rightarrow A_3$, and $A_3 \rightarrow A_4$) and a single Sp participates in several reactions as a module (Fig. 2b). For such a system, the magnitude of each $-\Delta_r G_i$ relative to the maximum $-\Delta_r G_i$ of all reactions, $\rho_i = -\Delta_r G_i / \max(-\Delta_r G_1, \ldots, -\Delta_r G_{Nreac})$, provides a measure of the degree of segmentation of the ith reaction within the template. ρ_i also shows the dependency of Sp i on others as Sp i that uses a reaction with significantly low ρ_i is unlikely to survive on its own.

In an ecological context, as each redox reaction can be regarded as a niche whose relative potential quality is given by ρ_i, Sp i using a high-quality reaction seems more likely to grow faster. However, despite the presence of reactions with larger ρ_i within the template, Sps using reactions with surprisingly smaller ρ_i often survived and consisted of pathways at a steady state (Fig. 2c). Under the given chemical and microbial conditions in Fig. 2c, Sp 8 occupied the most energetically favorable reaction

niche, whereas Sps 6, 19, and 41 using extremely low-quality segmented reactions survived at a steady state. Sps 19 and 41 were confirmed to even become extinct when each of them solely invaded the microbe-free system. Such an unexpected survival of Sps 19 and 41 can be deciphered by consecutively introducing each Sp out of the Sps that survived at the steady state to the microbe-free system to examine how interspecific interactions alter the reaction niches by connecting pathways (Fig. 2d). Although Sps 6, 19, and 41 negatively affect each other in terms of the utilization of C-bearing substances, the presence of Sp 6 is not sufficient but essential for the survival of Sps 19 and 41. This is because Sp 6 is a key cog to complete the cycle of A, improving the quality of the niches of Sps 19 and 41 by enhancing metabolic handoffs among A-bearing substances. Although the population growth of Sp *i* generally decreases the Gibbs energy of the system, the invasion of Sp *i* can improve other Sp's reaction niches by increasing the $-\Delta_r G$ of other Sps' energy source reactions. In particular, establishing a cyclic pathway tends to encourage the survival of Sp that uses a low-quality reaction niche.

The number of cycles in the established pathways at a steady state increases in response to the increase in the inflow of X_j when both electron acceptors and donors are supplied, which are possible at redox boundaries in natural systems (Fig. 3a). The excessive supply (or lack) of electrons depletes electron acceptors (or donors), during which the cycles are less likely to be established (Fig. 3b and c). The results are consistent with the observations at redox boundaries of natural aqueous systems or sediments where the supply of both electron donors and acceptors facilitates microbial material recycling and favors the growth of species that mutually operate those

reactions (Roden *et al.* 2004; Zerkle & Mikhail 2017). The increase in the number of cycles is accompanied by an increase in the number of Sps survived and a decline in ρ_i forming the established pathways. This suggests the facilitated division of labor into smaller units, even without assuming the trade-off between the yield and rate of ATP production (Fig. 3d). Hence, the supply of both electron donors and acceptors can enhance the division of labor that drive material cycles within a redox network.

An Sp using a reaction with smaller ρ_i may seem to only benefit from others. However, such Sp can play an essential role in the survival of the consortium that competes for Sp monopolizing the energetically more favorable reaction (Fig. 2a and b). For instance, the consortium of Sps 6, 19, 28, and 41 collectively proceed with $B_3 + C_2 \rightarrow B_2 + C_3$ (reaction 29), which outcompetes the Sp that exclusively harnesses reaction 29 and is more energetically favorable than segmented reactions. Such an entangling interplay is a good illustration of the survival strategy of microbes that form consortiums, whose growth would otherwise be thermodynamically limited (Bryant *et al.* 1967; Hoehler *et al.* 1994; Boetius *et al.* 2000). The results also explain the difficulty of isolating some species, especially chemolithoautotrophs harnessing reactions with lower $-\Delta_r G$. This is because the survival of those species might entirely depend on the co-presence of a key species that seems irrelevant and unhelpful but crucially supports the survival of the target species by modifying the material flow.

Predominance of the division of labor and thermodynamic efficiency

The topological structure of a redox network template determines the possible forms of division of labor. However, how do Sps with labor division confront Sps using

more energetically favorable reactions? The key strategy is to increase the thermodynamic efficiency to use more Gibbs energy as an assembly unit, which enhances ecosystem productivity. An illustrative example is a competition between Sps within a redox network at (N_A, N_B, N_C) = (2, 2, 2), where two Sps maximally survive. These two are either competitive or mutualistic, whereas the latter Sps (mutualistic Sps) also compete with the Sp monopolizing the complete reaction (monopoly Sp; see Fig. 2a). For an open system with the exchange of matter and/or energy, the Gibbs energy of the system deviates from the equilibrium G, G_{eq} (Fig. 4a). When Sp invades the system, the utilization of Gibbs energy brings G closer to G_{eq}, establishing G_{bio}. Letting the discrepancy between the steady-state G at the microbe-free state G_{abio}^* and G_{eq} be the net available Gibbs energy ($G_{abio}^* - G_{eq}$), we can define the thermodynamic efficiency of established pathways (η) as the ratio of the Gibbs energy utilized by the microbial community ($G_{abio}^* - G_{bio}$) to the net available Gibbs energy: $\eta = (G_{abio}^* - G_{bio})/(G_{abio}^* - G_{eq})$.

When a monopoly Sp and mutualistic Sps are separately introduced to the same microbe-free system, the Gibbs energy utilized by the monopoly Sp is often greater than that utilized by either of the mutualistic Sps solely (Fig. 4a). However, when both mutualistic Sps are present, they can efficiently utilize Gibbs energy by enhancing material cycle and thus lower G where the monopoly Sp can no longer survive (Fig. 4b). This relationship between G_{bio}^* and the competitive outcome is similar to the R^*-rule stating that a species that can establish the lowest abundance of resource at a steady state excludes others (Stewart & Levin 1973; Hsu *et al.* 1977;

Tilman 1977). Establishing pathways to better utilize the Gibbs energy would also be related to the maximum power (entropy production) principle, which predicts the direction of ecosystem development to maximize useful power (Odum & Pinkerton 1955; Nielsen *et al.* 2020). Figure 4c shows the Sp compositions that can establish the lowest G_{bio}^* at a steady state explored by the simulations for all possible Sp compositions. Monopoly Sp and mutualistic Sps competing for the same reaction niche do not coexist, and whichever can minimize G_{bio}^* survives and excludes the other. Meanwhile, Sps competing for the same reactant but not the same reaction niche can coexist, and the Sp combination that minimizes G_{bio}^* is not always achieved. The coexistence of competitive Sps often establishes higher G_{bio}^* than that established by each Sp *i* alone because they inhibit each other's growth.

Mutualistic Sps driving a material cycle can outcompete monopoly Sp at a larger inflow of X_j with well-balanced electron acceptors and donors. This leads to higher thermodynamic efficiency and biomass productivity (Fig. 5a and b). Mutualistic Sps also predominate when the catalytic abilities of all Sps are uniformly increased (Fig. S1). This result supports the selective advantage for species that utilizes a reaction with lower yield of ATP with a higher rate, even in the absence of the trade-off between the yield and rate of ATP production. The thermodynamic efficiency decreases with the increasing inflow rate of the most oxidized X_1, although the net available Gibbs energy ($G_{abio}^* - G_{eq}$) simultaneously increases. The decline in the thermodynamic efficiency is attributable to a kinetic (or f_i-limiting) constraint on the utilization of the Gibbs energy because of the resulting lack of electron donors. While the kinetic constraint decreases the thermodynamic efficiency, in some cases it prevents the overuse of the

Gibbs energy by preventing the G_{bio}^{*} from getting too close to G_{eq}, where microbial growth is self-regulated by the lack of energy, leading the lower biomass productivity.

For more complex networks, thermodynamic efficiency and total biomass can simultaneously increase in response to the increase in the number of cycles and Sps survived at a relatively lower inflow of X_j with a well-balanced supply of electron donors and acceptors (Fig. 5c and d). The result implies that, at the redox boundary under a limited supply of electron donors and acceptors, the species or functional diversity of microbes can support the ecosystem productivity because the replacement of monopolizing Sps by Sps with labor division leads to a more efficient use of the Gibbs energy.

Metabolic functional diversity and thermodynamic efficiency

The complexity of the redox network template in this study is inextricably linked to the diversity of microbial metabolic functions. As prokaryotes are thought to have gradually become able to harness diverse chemical reactions during their evolution (Nealson & Rye 2005), the redox network template would also have gradually become more complex in response to microbial metabolic functional diversity. For any thermodynamic and microbial conditions we explored, the increase in the complexity of the network template, characterized by the number of X_j participating in redox reactions N_{tot}, favors pathways that incorporate more cyclic structures with smaller ρ_i. This leads to higher thermodynamic efficiency and biomass productivity (Figs. 6). Sps with higher r_i and lower K_{i,X_j} were selected within a more complex network template because of the intensive competition. The established pathways incorporate more cycles than those established by Sps with constant r_i and K_{i,X_j} (cf. Figs. 6 and S2), which implies that

383 not only the metabolic diversity for the energy source but also the difference in
384 microbial catalytic abilities can enhance the division of labor that drives material cycles.
385
386 **Discussion**
387 Microbial life in a system with low energy supply has been considered to
388 employ two strategies for energy utilization. The first is energy conservation at an
389 individual level by lowering maintenance costs (Hoehler & Jørgensen 2013b; Lever *et*
390 *al.* 2015), while the second is energy use optimization by differentiating metabolic
391 pathways depending on the resource influx (Pfeiffer *et al.* 2001; Kreft *et al.* 2020).
392 Here, we propose a new strategy, an energy efficiency strategy at the community level:
393 microbial metabolic diversity can increase power generation through the enhancement
394 of division of labor, which accelerates material cycling through complex community
395 interactions, especially at redox boundaries where both electron donors and acceptors
396 are supplied in a balanced way.
397 Furthermore, our findings explain the ecological advantage of species using
398 reactions with low $-\Delta_r G$. These species appear to be tolerating the energetically harsh
399 environments, but can significantly impact on their ecosystem, like a keystone species.
400 Examples may include bacterial species harnessing nitrite oxidation with relatively
401 lower $-\Delta_r G$ (or lower ρ) in the nitrogen cycle. Nitrification occurs in two consecutive
402 steps (ammonia oxidation to nitrite and nitrite oxidation to nitrate) or in the complete
403 ammonia oxidation to nitrate (Daims *et al.* 2015). The advantage of nitrite oxidation has
404 often been discussed in terms of the competition with complete ammonia oxidation
405 (Costa *et al.* 2006); however, our study suggests that the survival strategy of nitrite-

406 oxidizing bacteria is rather to function as a key cog to form subcycles with nitrate
407 oxidation or denitrification.
408 The thermodynamic efficiency and the total biomass increased markedly with
409 an increase in metabolic diversity, especially when the supply of electron donors and
410 acceptors were balanced (Fig. 6b). This may be associated with the time interval
411 between the evolution of oxygenic photosynthetic organisms and the Great Oxidation
412 Event (GOE). Although the GOE is generally accepted to have been driven by the
413 evolution of oxygenic photosynthesis, oxygenic photosynthesis is thought to have
414 evolved a few hundred million to a few billion years before GOE (Planavsky *et al.*
415 2014; Ward *et al.* 2016). This time interval has traditionally been associated with
416 geological O_2 sinks, and a recent study suggested that the competitive outcome
417 between oxygenic and anoxygenic photosynthetic organisms may have contributed to
418 the timing of the GOE (Olejarz *et al.* 2021). Our study indicates that chemotrophic
419 communities may have served as missing sinks for O_2 as the increase in oxygen in the
420 relatively reduced atmosphere may have reached a quantity sufficient to drive redox
421 cycles, enabling chemotrophic microbial communities to proliferate. If microbial
422 metabolic diversity increases simultaneously, more oxygen could have been utilized
423 because of the enhanced thermodynamic efficiency and the productivity.
424 This study did not delve into the relationship between the thermodynamic
425 efficiency and the robustness of a microbial community. We confirmed the presence of
426 multistable steady states (see Section S3), each characterized by different species
427 compositions with different thermodynamic efficiencies. Intuitively, more productive
428 microbial communities with higher species diversity (or functional diversity) would be
429 robust to environmental disturbances. Furthermore, the microbial ecosystem

productivity would be maintained by the plastic responses of metabolic pathways (or species composition) that enable microbial communities to utilize the Gibbs energy at a reasonable thermodynamic efficiency.

The energy efficiency strategy at the community level is supported by the functional segmentation and differentiation of a microbial module, which would be particularly advantageous in fluctuating environments. However, in relatively stable environments, the shape of microbial metabolic pathways and species composition would also be stably maintained. The more constant and intimate interspecific interactions among unicellular cells in a consortium may have facilitated the evolutionary transition to a unicellular cell with more complex metabolic functions, such as aerobic respiration, and then eventually to a multicellular organism.

Acknowledgements

This study was supported by JSPS Grant-in-Aid for Scientific Research (C) Grant Numbers 19K06853 and 22K06390 (to MS) and by JSPS KAKENHI (JP19H05641 and JP21H05315) and the Environment Research and Technology Development Fund (JPMEERF20214103) of the Environmental Restoration and Conservation Agency of Japan (to MK). We thank the following people for their comments: Y. Iwasa, K. Kadowaki, and Y. Tachiki.

References

Anantharaman, K., Brown, C.T., Hug, L.A., Sharon, I., Castelle, C.J., Probst, A.J., *et al.*

(2016). Thousands of microbial genomes shed light on interconnected biogeochemical processes in an aquifer system. *Nature Communications*, 7.

Bar-On, Y.M., Phillips, R. & Milo, R. (2018). The biomass distribution on Earth. *Proceedings of the National Academy of Sciences*, 115, 6506–6511.

Boetius, A., Ravenschlag, K., Schubert, C.J., Rickert, D., Widdel, F., Gieseke, A., *et al.* (2000). A marine microbial consortium apparently mediating anaerobic oxidation of methane. *Nature*, 407, 623–626.

Bradley, J.A., Arndt, S., Amend, J.P., Burwicz, E., Dale, A.W., Egger, M., *et al.* (2020). Widespread energy limitation to life in global subseafloor sediments. *Science Advances*, 6, 1–9.

Bryant, M.P., Wolin, E.A., Wolin, M.J. & Wolfe, R.S. (1967). Methanobacillus omelianskii, a symbiotic association of two species of bacteria., 59, 20–31.

Costa, E., Pérez, J. & Kreft, J.U. (2006). Why is metabolic labour divided in nitrification? *Trends in Microbiology*, 14, 213–219.

Daims, H., Lebedeva, E. V., Pjevac, P., Han, P., Herbold, C., Albertsen, M., *et al.* (2015). Complete nitrification by Nitrospira bacteria. *Nature*, 528, 504–509.

469 Embree, M., Liu, J.K., Al-Bassam, M.M. & Zengler, K. (2015). Networks of energetic
470 and metabolic interactions define dynamics in microbial communities. *Proceedings*
471 *of the National Academy of Sciences of the United States of America*, 112, 15450–
472 15455.
473 Falkowski, P.G., Fenchel, T. & Delong, E.F. (2008). The microbial engines that drive
474 Earth's biogeochemical cycles. *Science*, 320, 1034–1039.
475 Flemming, H.C. & Wuertz, S. (2019). Bacteria and archaea on Earth and their
476 abundance in biofilms. *Nature Reviews Microbiology*, 17, 247–260.
477 Hoehler, T.M., Alperin, M.J., Albert, D.B. & Martens, C.S. (1994). Field and laboratory
478 studies of methane oxidation in an anoxic marine sediment: Evidence for a
479 methanogen-sulfate reducer consortium. *Global Biogeochemical Cycles*, 8, 878–
480 879.
481 Hoehler, T.M. & Jørgensen, B.B. (2013a). Microbial life under extreme energy
482 limitation. *Nat. Rev. Microbiol.*, 11, 83–94.
483 Hoehler, T.M. & Jørgensen, B.B. (2013b). Microbial life under extreme energy
484 limitation. *Nature Reviews Microbiology*.

485 Hsu, S.B., Hubble, S. & Waitman, P. (1977). A mathematical theory of single-nutrient
486 competition in continuous cultures of micro-organisms. *SIAM J. Appl. Math.*, 32,
487 366–383.
488 Jørgensen, B.B. & Boetius, A. (2007). Feast and famine - Microbial life in the deep-sea
489 bed. *Nature Reviews Microbiology*, 5, 770–781.
490 Kallmeyer, J., Pockalny, R., Adhikari, R.R., Smith, D.C. & D'Hondt, S. (2012). Global
491 distribution of microbial abundance and biomass in subseafloor sediment.
492 *Proceedings of the National Academy of Sciences of the United States of America*,
493 109, 16213–16216.
494 Kouzuma, A., Kato, S. & Watanabe, K. (2015). Microbial interspecies interactions:
495 Recent findings in syntrophic consortia. *Frontiers in Microbiology*.
496 Kreft, J.U., Griffin, B.M. & González-Cabaleiro, R. (2020). Evolutionary causes and
497 consequences of metabolic division of labour: why anaerobes do and aerobes
498 don't. *Current Opinion in Biotechnology*.
499 Kuypers, M.M.M., Marchant, H.K. & Kartal, B. (2018). The microbial nitrogen-cycling
500 network. *Nature Reviews Microbiology*.

Lever, M.A., Rogers, K.L., Lloyd, K.G., Overmann, J., Schink, B., Thauer, R.K., *et al.* (2015). Life under extreme energy limitation: A synthesis of laboratory- and field-based investigations. *FEMS Microbiology Reviews*.

Magnabosco, C., Lin, L.H., Dong, H., Bomberg, M., Ghiorse, W., Stan-Lotter, H., *et al.* (2018). The biomass and biodiversity of the continental subsurface. *Nature Geoscience*, 11, 707–717.

McInerney, M.J., Sieber, J.R. & Gunsalus, R.P. (2009). Syntrophy in anaerobic global carbon cycles. *Current Opinion in Biotechnology*, 20, 623–632.

Momper, L., Jungbluth, S.P., Lee, M.D. & Amend, J.P. (2017). Energy and carbon metabolisms in a deep terrestrial subsurface fluid microbial community. *ISME Journal*, 11, 2319–2333.

Morono, Y., Terada, T., Nishizawa, M., Ito, M., Hillion, F., Takahata, N., *et al.* (2011). Carbon and nitrogen assimilation in deep subseafloor microbial cells. *Proceedings of the National Academy of Sciences*, 201107763.

Morris, B.E.L., Henneberger, R., Huber, H. & Moissl-Eichinger, C. (2013). Microbial syntrophy: Interaction for the common good. *FEMS Microbiology Reviews*, 37,

384–406.

Nealson, K.H. & Rye, R. (2005). *Evolution of Metabolism*. *Biogeochemistry (ed. W.H. Schlesinger) Vol.8 Treatise on Geochemistry (eds. H.D. Holland and K.K. Turekian)*. Elsevier-Pergamon, Oxford.

Nielsen, S.N., Müller, F., Marques, J.C., Bastianoni, S. & Jørgensen, S.E. (2020). Thermodynamics in ecology-An introductory review. *Entropy*, 22.

Odum, H.T. & Pinkerton, R.C. (1955). Time's speed regulator: the optimum efficiency for maximum power output in physical and biological systems. *American Scientist*, 43.

Olejarz, J., Iwasa, Y., Knoll, A.H. & Nowak, M.A. (2021). The Great Oxygenation Event as a consequence of ecological dynamics modulated by planetary change. *Nature Communications*, 12.

Pfeiffer, T., Schuster, S. & Bonhoeffer, S. (2001). Cooperation and competition in the evolution of ATP-producing pathways. *Science*, 292, 504–507.

Planavsky, N.J., Asael, D., Hofmann, A., Reinhard, C.T., Lalonde, S. V., Knudsen, A., *et al.* (2014). Evidence for oxygenic photosynthesis half a billion years before the

533 Great Oxidation Event. *Nature Geoscience*, 7.

534 Roden, E.E., Sobolev, D., Glazer, B. & Luther, G.W. (2004). Potential for Microscale

535 Bacterial Fe Redox Cycling at the Aerobic-Anaerobic Interface. *Geomicrobiology*

536 *Journal*, 21, 379–391.

537 Seto, M. & Iwasa, Y. (2019a). Population dynamics of chemotrophs in anaerobic

538 conditions where the metabolic energy acquisition per redox reaction is limited.

539 *Journal of Theoretical Biology*, 467.

540 Seto, M. & Iwasa, Y. (2019b). The fitness of chemotrophs increases when their

541 catabolic by-products are consumed by other species. *Ecology Letters*, 22, 1994–

542 2005.

543 Seto, M. & Iwasa, Y. (2020). Microbial material cycling, energetic constraints and

544 ecosystem expansion in subsurface ecosystems. *Proceedings of the Royal Society*

545 *B: Biological Sciences*, 287, 20200610.

546 Starnawski, P., Bataillon, T., Ettema, T.J.G., Jochum, L.M., Schreiber, L., Chen, X., *et*

547 *al.* (2017). Microbial community assembly and evolution in subseafloor sediment.

548 *Proceedings of the National Academy of Sciences of the United States of America*,

201614190.

Stewart, F.M. & Levin, B.R. (1973). Partitioning of Resources and the Outcome of Interspecific Competition: A Model and Some General Considerations. *The American Naturalist*, 107, 171–198.

Tilman, D. (1977). Resource Competition between planktonic algae: an experimental and theoretical approach. *Ecology*, 58, 338–348.

Ward, L.M., Kirschvink, J.L. & Fischer, W.W. (2016). Timescales of Oxygenation Following the Evolution of Oxygenic Photosynthesis. *Origins of Life and Evolution of Biospheres*, 46.

Zerkle, A.L. & Mikhail, S. (2017). The geobiological nitrogen cycle: From microbes to the mantle. *Geobiology*, 15.

Figure legends

Fig. 1 | Outline of the eco-redox model. **a.** The redox network template and its material network when (N_A, N_B, N_C) = (2, 2, 2) and (N_A, N_B, N_C) = (4, 4, 4). *i* in the smaller nodes denotes the energy-source reaction for Sp *i*. Blue and red arrows correspond to oxidation and reduction reactions, respectively (solid for reaction 1 and dotted for reaction 4, the reverse reaction of reaction 1). **b.** Thermodynamic advantage

of the *i*th reaction weighted by the negative of the Gibbs energy change of reaction ($-\Delta_r G_i$). **c.** Microbially established pathways at a steady state within the same redox network template composed of X_j with different standard chemical potentials. For **b** and **c**, the sizes of the nodes are weighted by the chemical potential of X_j at a steady state.

Fig. 2 | Division of labor within a redox network. a. Interspecific relationships among three Sps and the competitive relationship between Sps with labor division and Sp using a complete reaction within the redox network template at (N_A, N_B, N_C) = (2, 2, 2). **b.** Examples of complex division of labor and the degree of segmentation of the *i*th redox reaction, $\rho_i = -\Delta_r G_i/\max.(-\Delta_r G_1, \ldots, -\Delta_r G_{Nreac})$. **c.** An example of the dynamics within a redox template consisting of 60 reactions and the same number of Sps at (N_A, N_B, N_C) = (3, 3, 3). The edges in the upper and lower network diagrams are weighted by the degree of segmentation and the flow rate ($f_i M_i + F_i$) at t = 0, 10, and 2000, respectively. The nodes representing X_j are weighted by the chemical potential of X_j at each t. The table summarizes the values of $-\Delta_r G_i$ and ρ_i of the microbial pathways established at a steady state. **d.** The dynamics when each of the Sps that survived at the steady state in **c** was consecutively introduced to a microbe-free system. The nodes representing X_j are weighted by the chemical potential of X_j at a steady state. The values of the thermodynamic, kinetic, and microbial parameters used for **c** are provided in csv files along with a sample program written in Wolfram language (see Supporting Information S2.2).

Fig. 3 | Establishment of cyclic pathways and division of labor at a steady state at

590 **(N_A, N_B, N_C) = (4, 4, 4). a**. Average number of cycles established in response to the
591 change in the inflow rate of all X_j (I_{X_j} = [Inflow rate]/N_{tot} shown by solid lines) and
592 only the most oxidized X_1 (I_{X_1} = [Inflow rate] and 10^{-5} for other I_{X_j} shown by
593 dotted lines), respectively, with 1000 iterations for each inflow rate. **b** Number of
594 established cycles at various redox balances when the values of I_{X_j} were randomly
595 selected at a fixed total inflow rate ($\sum_X \sum_j I_{X_j} = 10^{-3}$), with 5000 iterations. The redox
596 balance of the inflow was estimated by balancing the abundance of electron acceptors
597 and donors in the inflow. **c.** Probability of the established pathways possessing no cycles
598 and four cycles at varying I_{X_j}, with 20000 iterations. **d**. Average of the number of Sps
599 (left) and the minimum of ρ_i (right) of the established pathways with x cycles to the
600 change in the inflow rate of all X_j (I_{X_j} = [Inflow rate]/N_{tot}), with 1000 iterations for
601 each inflow rate. The values of other parameters and ranges for random variables are
602 summarized in Table S1. The error bars show 2 SE in **a** and **d** and the maximum and
603 minimum values in **b**.
604
605 **Fig. 4 | Competitive outcome between a monopolizing Sp (Sp 1) and mutualistic**
606 **Sps with labor division (Sps 2 and 3) and the utilization of Gibbs energy at (N_A, N_B,**
607 **N_C) = (2, 2, 2). a.** Dynamics of microbial growth (top left and right), Gibbs energy G
608 (down left), and thermodynamic efficiency η (down right) when a monopoly Sp was
609 solely (top left) and mutualistic Sps were sequentially (top right) introduced to the same
610 microbe-free environment. There were no inflow and outflow at $0 \leq t < 1000$. **b**.
611 Dynamics of microbial growth when Sps 1-3 were introduced to the microbe-free
612 system at $t = 0$. **c**. Combination of Sps that established the lowest G_{bio}^* (left) and Sps

that survived at a steady state (right) in response to the change in the inflow rates of B_1 and B_2. The parameters and initial values are shown in Table S2.

Fig. 5 | Steady-state total biomass and thermodynamic efficiency in response to the inflow rate of X_j at (N_A, N_B, N_C) = (2, 2, 2) (a, b) and at (N_A, N_B, N_C) = (4, 4, 4) (c, d). a. The responses of the types of interspecific relationships (top), thermodynamic efficiency (middle), and total biomass (bottom) to the change in the inflow rate of all X_j (I_{X_j} = [Inflow rate]/N_{tot}) (left) and only the most oxidized X_1 (I_{X_1} = [Inflow rate] and 10^{-5} for other I_{X_j}) (right). **b.** The relationship between the total biomass and thermodynamic efficiency at $I_{X_j} = 10^{-6}/6$ for all X_j. For **a** and **b**, black, red, and blue show the steady state where monopoly Sp only exists, competitive two Sps coexist, and mutualistic two Sps coexist, respectively. **c.** The responses of the thermodynamic efficiency (top) and total biomass (bottom) to the change in the inflow rate of all X_j (I_{X_j} = [Inflow rate]/N_{tot} shown by solid lines) and only the most oxidised X_1 (I_{X_1} = [Inflow rate] and 10^{-5} for other I_{X_j} shown by dotted lines). **d.** Relationships between the thermodynamic efficiency and the number of Sps (top left), the thermodynamic efficiency and the number of cycles (top right), the total biomass normalized by the total inflow rate ($\sum_i M_i^* / \sum_X \sum_j I_{X_j}$) and the number of Sps (bottom left), and the total biomass normalized by the total inflow rate and the number of cycles (bottom right) at different inflow rate (I_{X_j}) of all X_j. Other parameters were set to the default values shown in Table S1. The simulation was iterated 1000 times for each inflow rate. The error bars show 2 SE.

Fig. 6 | Steady-state responses to changes in the inflow rate and the redox network template complexity as microbial functional complexity. a, b. Steady-state responses at different inflow rates of all X_j ($I_{X_j} =$ [Inflow rate]/N_{tot}) (**a**) and only the most oxidised X_1 ($I_{X_1} =$ [Inflow rate] and 10^{-5} for other I_{X_j}) (**b**) at different levels of the redox network template complexity characterized by the total number of X-bearing chemical species (N_{tot}) utilized by microbes. (Top left) Average of the number of cycles; (top right) the minimum degree of segmentation; (middle left) thermodynamic efficiency; (middle right) total biomass normalized by the total inflow rate ($\sum_i M_i^* / \sum_X \sum_j I_{X_j}$); (bottom left and right) microbial catalytic rate and Michaelis-Menten constant of Sps survived at steady state. For **b**, the redox condition of inflow is the most balanced at $\log_{10} I_{X_j} = -5$. The simulations at a given inflow rate and N_{tot} condition were repeated 1000 times. Other parameters were set to the default values shown in Table S1.

Competing interests

The authors declare no competing interests.

Supplementary Information is available for this paper.

Correspondence and requests for materials should be addressed to Mayumi Seto

658

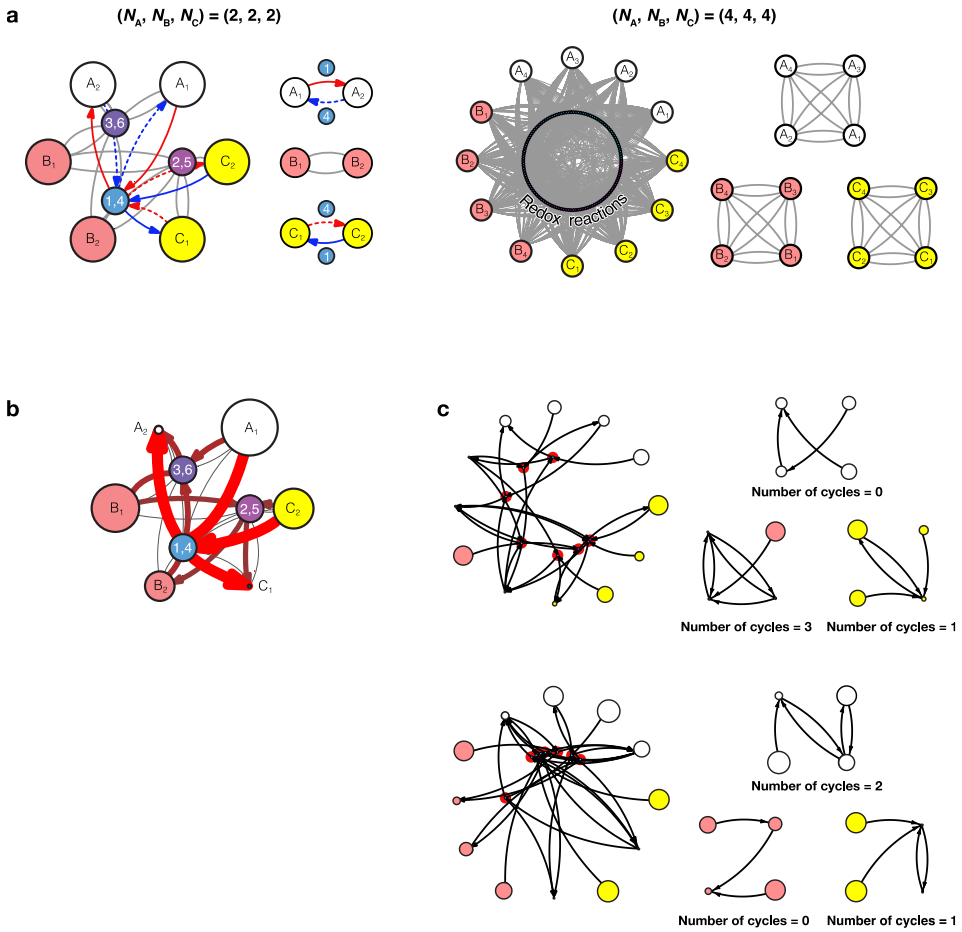

Fig. 1 | Outline of the eco-redox model. **a.** The redox network template and its material network when (N_A, N_B, N_C) = (2, 2, 2) and (N_A, N_B, N_C) = (4, 4, 4). *i* in the smaller nodes denotes the energy-source reaction for Sp *i*. Blue and red arrows correspond to oxidation and reduction reactions, respectively (solid for reaction 1 and dotted for reaction 4, the reverse reaction of reaction 1). **b.** Thermodynamic advantage of the *i*th reaction weighted by the negative of the Gibbs energy change of reaction ($-\Delta_r G_i$). **c.** Microbially established pathways at a steady state within the same redox network template composed of X_j with different standard chemical potentials. For **b** and **c**, the sizes of the nodes are weighted by the chemical potential of X_j at a steady state.

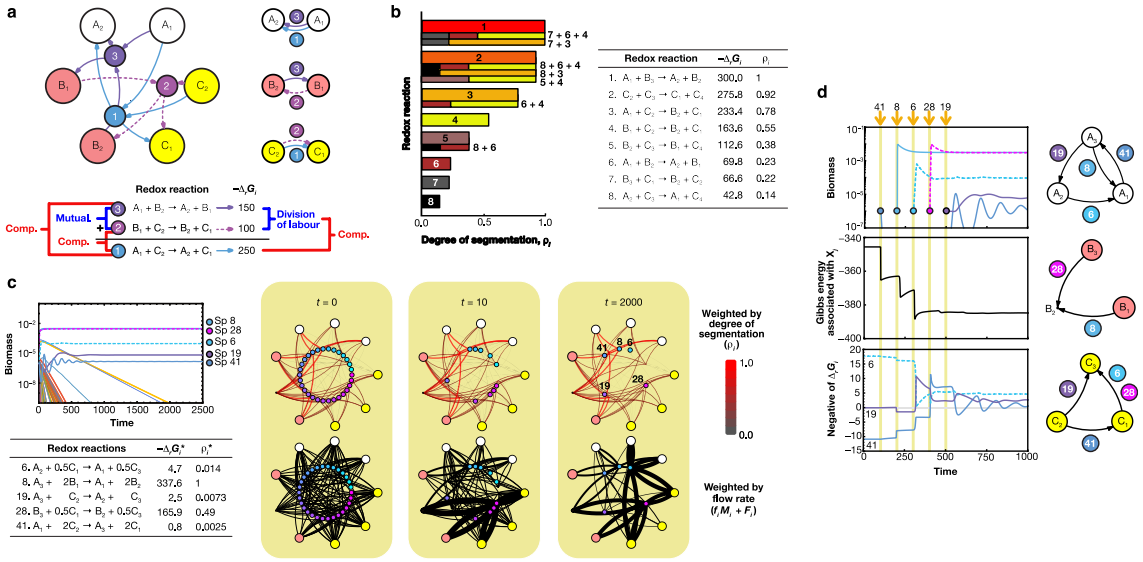

Redox reaction	$-\Delta_r G_i$	ρ_i
1. $A_1 + B_2 \rightarrow A_2 + B_2$	300.0	1
2. $C_2 + C_2 \rightarrow C_1 + C_1$	275.8	0.92
3. $A_1 + C_2 \rightarrow B_2 + C_1$	233.4	0.78
4. $B_1 + C_2 \rightarrow B_2 + C_1$	163.6	0.55
5. $B_2 + C_2 \rightarrow B_1 + C_1$	112.6	0.38
6. $A_1 + B_2 \rightarrow A_2 + B_1$	69.8	0.23
7. $B_2 + C_2 \rightarrow B_2 + C_2$	66.6	0.22
8. $A_2 + C_2 \rightarrow A_2 + C_1$	42.8	0.14

Redox reactions	$-\Delta_r G_i^*$	ρ_i^*
6. $A_2 + 0.5C_2 \rightarrow A_2 + 0.5C_2$	4.7	0.014
8. $A_2 + 2B_2 \rightarrow A_2 + 2B_2$	337.6	1
19. $A_2 + C_2 \rightarrow A_2 + C_2$	2.5	0.0073
28. $B_2 + 0.5C_2 \rightarrow B_2 + 0.5C_2$	165.9	0.49
41. $A_2 + 2C_2 \rightarrow A_2 + 2C_2$	0.8	0.0025

Fig. 2 | Division of labor within a redox network. a. Interspecific relationships among three Sps and the competitive relationship between Sps with labor division and Sp using a complete reaction within the redox network template at (N_A, N_B, N_C) = (2, 2, 2). **b.** Examples of complex division of labor and the degree of segmentation of the ith redox reaction, $\rho_i = -\Delta_r G_i/\max.(-\Delta_r G_1, \ldots, -\Delta_r G_{Nreac})$. **c.** An example of the dynamics within a redox template consisting of 60 reactions and the same number of Sps at (N_A, N_B, N_C) = (3, 3, 3). The edges in the upper and lower network diagrams are weighted by the degree of segmentation and the flow rate ($f_i M_i + F_i$) at t = 0, 10, and 2000, respectively. The nodes representing X_j are weighted by the chemical potential of X_j at each t. The table summarizes the values of $-\Delta_r G_i$ and ρ_i of the microbial pathways established at a steady state. **d.** The dynamics when each of the Sps that survived at the steady state in **c** was consecutively introduced to a microbe-free system. The nodes representing X_j are weighted by the chemical potential of X_j at a steady state. The values of the thermodynamic, kinetic, and microbial parameters used for **c** are provided in csv files along with a sample program written in Wolfram language (see Supporting Information S2.2).

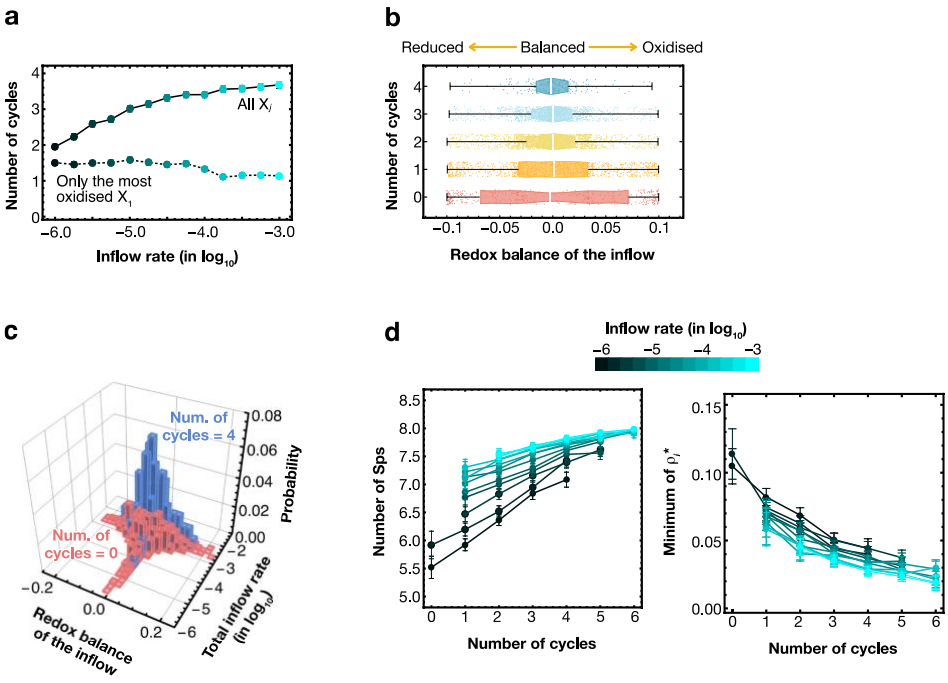

Fig. 3 | Establishment of cyclic pathways and division of labor at a steady state at (N_A, N_B, N_C) = (4, 4, 4). a. Average number of cycles established in response to the change in the inflow rate of all X_j (I_{X_j} = [Inflow rate]/N_{tot} shown by solid lines) and only the most oxidized X_1 (I_{X_1} = [Inflow rate] and 10^{-5} for other I_{X_j} shown by dotted lines), respectively, with 1000 iterations for each inflow rate. **b** Number of established cycles at various redox balances when the values of I_{X_j} were randomly selected at a fixed total inflow rate ($\sum_X \sum_j I_{X_j} = 10^{-3}$), with 5000 iterations. The redox balance of the inflow was estimated by balancing the abundance of electron acceptors and donors in the inflow. **c.** Probability of the established pathways possessing no cycles and four cycles at varying I_{X_j}, with 20000 iterations. **d**. Average of the number of Sps (left) and the minimum of ρ_i (right) of the established pathways with x cycles to the change in the inflow rate of all X_j (I_{X_j} = [Inflow rate]/N_{tot}), with 1000 iterations for each inflow rate. The values of other parameters and ranges for random variables are summarized in Table S1. The error bars show 2 SE in **a** and **d** and the maximum and minimum values in **b**.

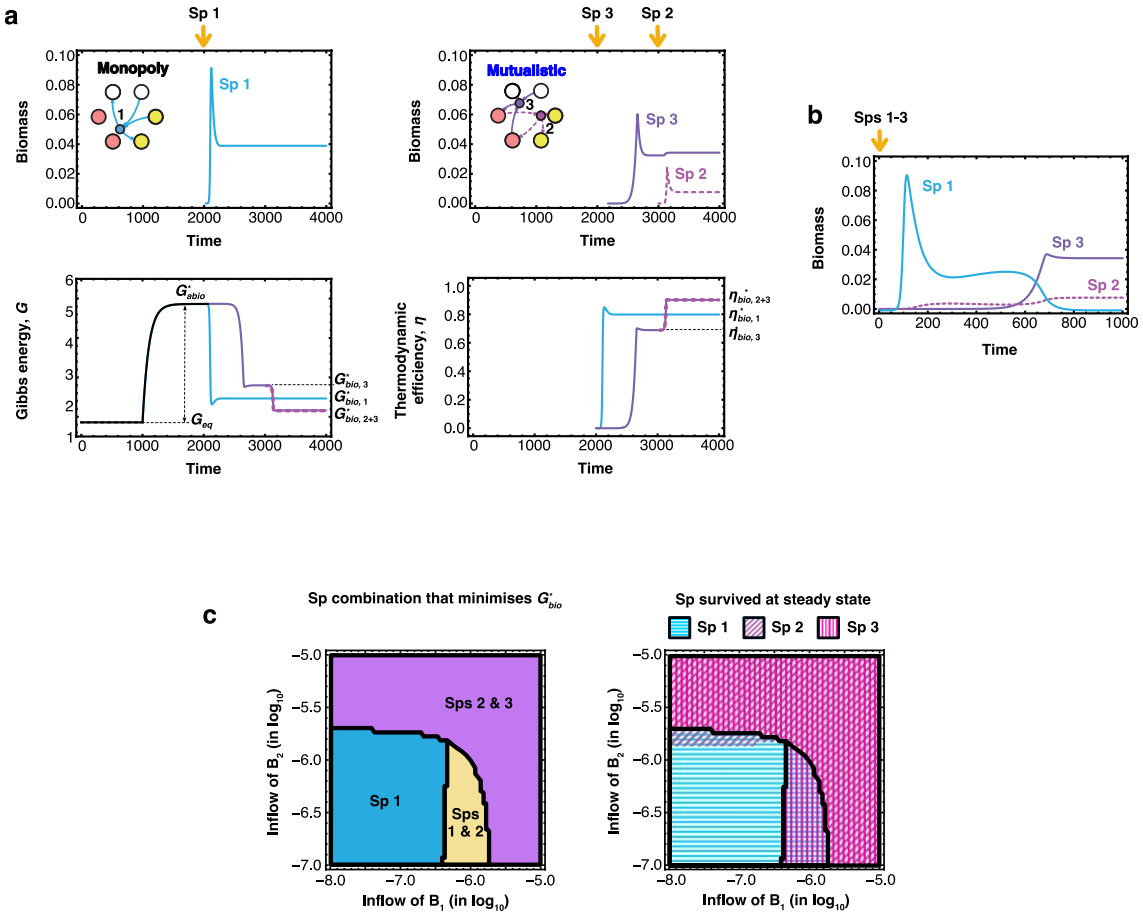

Fig. 4 | Competitive outcome between a monopolizing Sp (Sp 1) and mutualistic Sps with labor division (Sps 2 and 3) and the utilization of Gibbs energy at (N_A, N_B, N_C) = (2, 2, 2). a. Dynamics of microbial growth (top left and right), Gibbs energy G (down left), and thermodynamic efficiency η (down right) when a monopoly Sp was solely (top left) and mutualistic Sps were sequentially (top right) introduced to the same microbe-free environment. There were no inflow and outflow at $0 \leq t < 1000$. **b.** Dynamics of microbial growth when Sps 1-3 were introduced to the microbe-free system at $t = 0$. **c.** Combination of Sps that established the lowest G_{bio}^* (left) and Sps that survived at a steady state (right) in response to the change in the inflow rates of B_1 and B_2. The parameters and initial values are shown in Table S2.

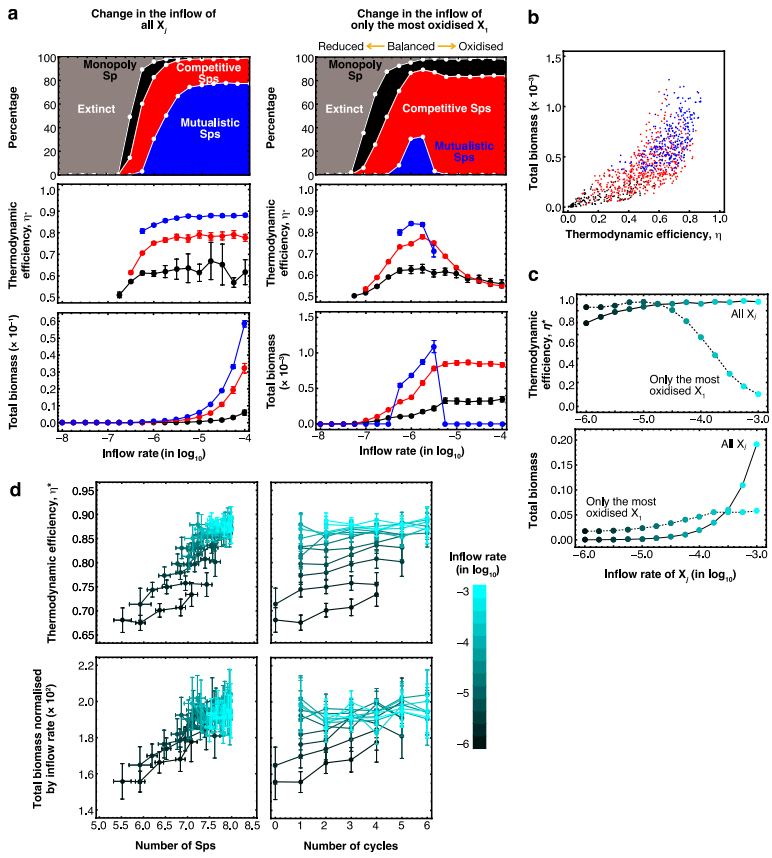

Fig. 5 | Steady-state total biomass and thermodynamic efficiency in response to the inflow rate of X_j at (N_A, N_B, N_C) = (2, 2, 2) (a, b) and at (N_A, N_B, N_C) = (4, 4, 4) (c, d). a. The responses of the types of interspecific relationships (top), thermodynamic efficiency (middle), and total biomass (bottom) to the change in the inflow rate of all X_j (I_{X_j} = [Inflow rate]/N_{tot}) (left) and only the most oxidized X_1 (I_{X_1} = [Inflow rate] and 10^{-5} for other I_{X_j}) (right). **b.** The relationship between the total biomass and thermodynamic efficiency at $I_{X_j} = 10^{-6}/6$ for all X_j. For **a** and **b**, black, red, and blue show the steady state where monopoly Sp only exists, competitive two Sps coexist, and mutualistic two Sps coexist, respectively. **c**. The responses of the thermodynamic efficiency (top) and total biomass (bottom) to the change in the inflow rate of all X_j (I_{X_j} = [Inflow rate]/N_{tot} shown by solid lines) and only the most oxidised X_1 (I_{X_j} = [Inflow rate]/N_{tot}). **d**. Relationships between the thermodynamic efficiency and the number of Sps (top left), the thermodynamic efficiency and the number of cycles (top right), the total biomass normalized by the total inflow rate ($\sum_i M_i^* / \sum_X \sum_j I_{X_j}$) and the number of Sps (bottom left), and the total biomass normalized by the total inflow rate and the number of cycles (bottom right) at different inflow rate (I_{X_j}) of all X_j. Other parameters were set to the default values shown in Table S1. The simulation was iterated 1000 times for each inflow rate. The error bars show 2 SE.

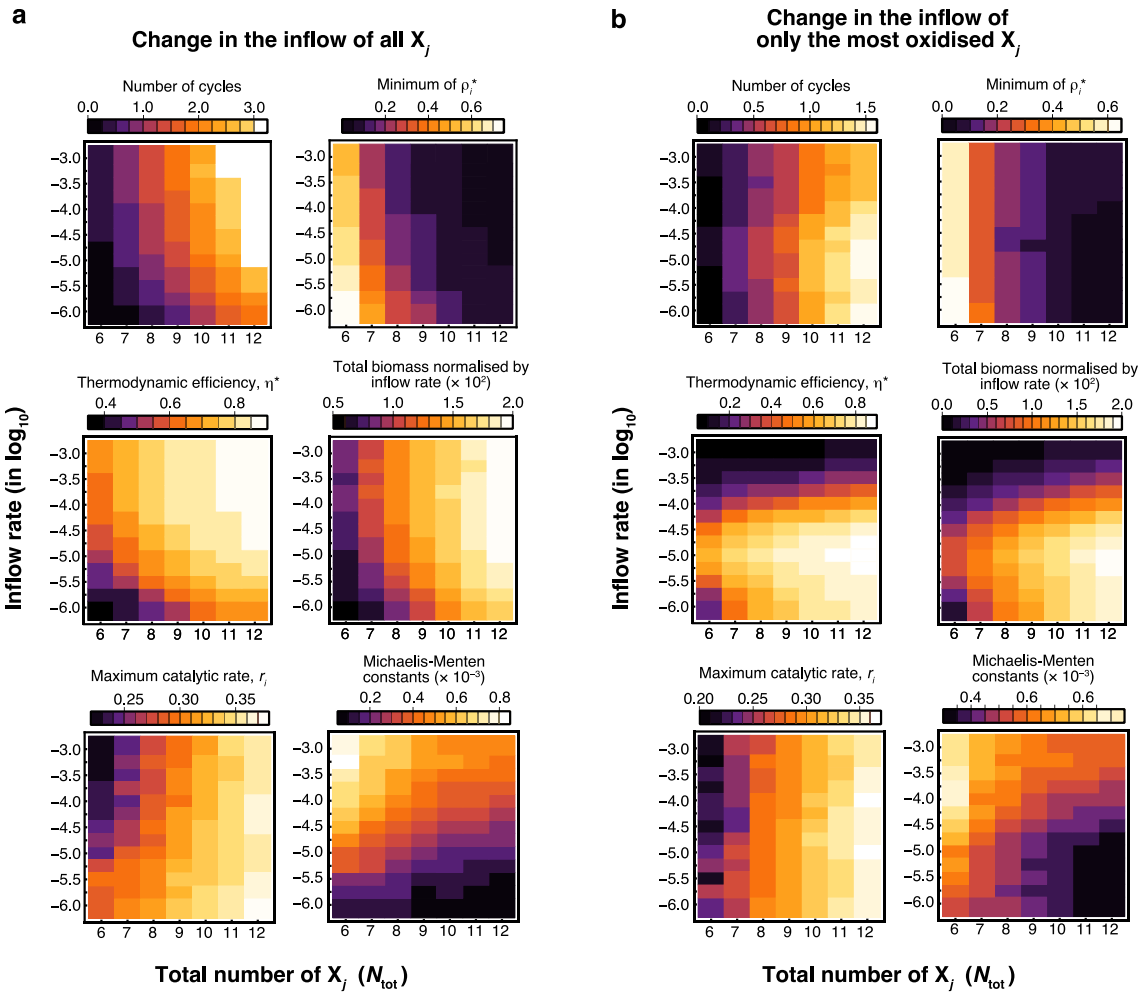

Fig. 6 | Steady-state responses to changes in the inflow rate and the redox network template complexity as microbial functional complexity. a, b. Steady-state responses at different inflow rates of all X_j ($I_{X_j} =$ [Inflow rate]/N_{tot}) (**a**) and only the most oxidised X_1 ($I_{X_1} =$ [Inflow rate] and 10^{-5} for other I_{X_j}) (**b**) at different levels of the redox network template complexity characterized by the total number of X-bearing chemical species (N_{tot}) utilized by microbes. (Top left) Average of the number of cycles; (top right) the minimum degree of segmentation; (middle left) thermodynamic efficiency; (middle right) total biomass normalized by the total inflow rate ($\sum_i M_i^* / \sum_X \sum_j I_{X_j}$); (bottom left and right) microbial catalytic rate and Michaelis-Menten constant of Sps survived at steady state. For **b**, the redox condition of inflow is the most balanced at $\log_{10} I_{X_j} = -5$. The simulations at a given inflow rate and N_{tot} condition were repeated 1000 times. Other parameters were set to the default values shown in Table S1.